Research article

Fluid-structure interaction simulation of calcified aortic valve stenosis

Li Cai[1,2,3]**, Yu Hao**[1,2,3,*]**, Pengfei Ma**[1,2,3]**, Guangyu Zhu**[4]**, Xiaoyu Luo**[5] **and Hao Gao**[5,*]

[1] School of Mathematics and Statistics, Northwestern Polytechnical University, Xi'an 710129, China

[2] NPU-UoG International Cooperative Lab for Computation and Application in Cardiology, Xi'an 710129, China

[3] Xi'an Key Laboratory of Scientific Computation and Applied Statistics, Xi'an 710129, China

[4] School of Energy and Power Engineering, Xi'an Jiaotong University, Xi'an 710049, China

[5] School of Mathematics and Statistics, University of Glasgow, Glasgow, G12 8QQ, UK

* **Correspondence:** Email: yuhao_nwpu@163.com, hao.gao@glasgow.ac.uk.

Abstract: Calcified aortic valve stenosis (CAVS) is caused by calcium buildup and tissue thickening that impede the blood flow from left ventricle (LV) to aorta. In recent years, CAVS has become one of the most common cardiovascular diseases. Therefore, it is necessary to study the mechanics of aortic valve (AV) caused by calcification. In this paper, based on a previous idealized AV model, the hybrid immersed boundary/finite element method (IB/FE) is used to study AV dynamics and hemodynamic performance under normal and calcified conditions. The computational CAVS model is realized by dividing the AV leaflets into a calcified region and a healthy region, and each is described by a specific constitutive equation. Our results show that calcification can significantly affect AV dynamics. For example, the elasticity and mobility of the leaflets decrease due to calcification, leading to a smaller opening area with a high forward jet flow across the valve. The calcified valve also experiences an increase in local stress and strain. The increased loading due to AV stenosis further leads to a significant increase in left ventricular energy loss and transvalvular pressure gradients. The model predicted hemodynamic parameters are in general consistent with the risk classification of AV stenosis in the clinic. Therefore, mathematical models of AV with calcification have the potential to deepen our understanding of AV stenosis-induced ventricular dysfunction and facilitate the development of computational engineering-assisted medical diagnosis in AV related diseases.

Keywords: fluid-structure interaction; aortic valve; calcification; hybrid immersed boundary/finite element method

1. Introduction

The etiology of aortic valve (AV) stenosis can be classified as congenital, rheumatic and calcific, in which calcification is the main and most common cause [1, 2]. In Western countries, calcified aortic valve stenosis (CAVS) has become the third leading cardiovascular disease after coronary heart disease and elderly hypertension [3]. Calcification increases with age and affects mainly the older, occurring in 2–7% of people over age of 65 [4]. Once clinical symptoms appear, non-surgical treatment has a poor prognosis with a 2-year survival rate of only 50%. Currently, the most common treatment is valve replacement with a mechanical or biological valve [5, 6]. Furthermore, calcification is also a major cause of the failure of bioprostheses [7]. Long-term follow-up studies have found that the incidence of structural valve degeneration 15 years after implantation is 30% to 60%, which is partly caused by calcification [8].

Calcification has been previously thought to be a passive process of calcium deposition on valve over time [9]. However, recent studies have shown that it is the result of active regulation by multiple factors such as inflammation and metabolism. Beginning with subclinical inflammation, it progresses through stages of fibrosis and leaflet thickening, culminating in valve calcification [10]. Calcification alters the geometry and material properties of the AV, resulting in reduced flexibility and opening area that block the flow of blood from the left ventricle (LV) to the aorta. To supply the body with required volume of oxygenated blood, the heart self-regulates pump function by increasing its contractility to maintain the cardiac output.

Healthy AV has mechanical properties of anisotropy, nonlinearity, incompressibility and hyperelasticity. Since calcification is a dynamic growth process and is not evenly distributed on the leaflets, which will change the material properties of the valve. AV calcification has been mathematically modeled in various ways, such as by changing the parameters of its constitutive equation, or increasing the thickness of the leaflets, or increasing the stiffness of calcified region. For example, Mutlu et al. [11] used linear elastic material model to simulate calcification levels with different elastic moduli to study complex regional flow in healthy and calcified AVs. Using the same calcification assumptions, Kivi et al. [12] studied the hemodynamic effects of calcification on the aortic root and coronary arteries to identify potential onset sites of coronary stenosis in a two-dimensional healthy AV model. Luraghi et al. [13] reconstructed a 3D model of the aortic root and calcium deposits from CT images of patients, numerical simulations were performed on 7 patients using the Lagrangian-Eulerian method. Halevi et al. [14, 15] proposed a new method of reverse calcification process, which could reconstruct different stages of calcification to study its effects on valve hemodynamics. Maleki et al. [16] introduced an indicator (a parameter of the constitutive equation) whose value was varied to scale the overall elastic response of the valve tissue according to the severity of Calcification. Assuming the calcification process occurring in the high-strain region, Arzani et al. [17] developed a finite element model of the calcification process where calcification was modelled by increasing the stiffness of the affected region. To simulate the reduced mobility of leaflets due to calcification, Meschini et al. [18] immobilized parts of the area close to the mitral valve(MV) root, and the calcification severity was determined by the area of the calcification. Subsequently, different degrees of stenosis of AV were investigated using a fluid-structure-electrophysiology approach and calcification was modelled in a similar way as in [19].

Finite Element (FE) method [20, 21], Arbitrary Lagrangian-Eulerian (ALE) method [22, 23], fictitious domain (FD) method [24] and immersed boundary (IB) method [25–28] are widely used to deal

with fluid-structure interaction (FSI) problems [29]. Because the IB method does not need to generate dynamic body-fitted meshes that greatly simplifies mesh generation, and thus is often used for numerical simulation of large deformation elastic solids. Griffith and Luo [30] proposed the hybrid finite difference/finite element immersed boundary (IB/FE) method based on the IB method, which uses finite element discretization for immersed structures and finite difference discretization for incompressible Navier-Stokes equations. It can overcome one long-standing issue that the Euler grid is twice as fine when the Lagrangian grid is required under the conventional IB method to prevent leakage of the fluid-structure interaction interface. Gao et al. [28] used this IB/FE framework to study a personalized human mitral valve dynamics under physiological pressure loads and then extended it to a coupled MV-LV model [31]. Hasan et al. [32] developed aortic root and ascending aorta models from computed tomography angiography, and the results were consistent with clinical data. Recently, Cai et al. [33, 34] investigated the effect of different constitutive equations on the dynamics of AV and MV using the same IB/FE modelling framework. Other applications of the IB/FE approach can be found in [35–37].

In this paper, based on the assumption that calcification develops from the medial to the free end of the aortic valve [38], regional-varied constitutive equations are adopted to study calcified and healthy valves. The IB/FE method is used to simulate AV dynamics with fluid-structure interaction. Finally, the AV dynamics and selected hemodynamic parameters are analyzed at different calcification severity.

2. Methods

2.1. Geometric model and constitutive laws of AV leaflets

In this study, the geometric model of healthy AV is adapted from our previous study [34], which was constructed from a porcine pericardial valve with a leaflet thickness of 0.04 cm [39], shown in Figure 1(a). The AV is mounted in a straight pipe that has a total length of 13 cm with inner radius of 1.3 cm and wall thickness of 0.15 cm.

Thubrikar et al. [38] have reported calcification patterns in surgically resected end-stage calcified valves, showing calcium deposits in the cusps and commissures with a radial spread to the abdominal region. The physiological anatomy reported by Otto et al. [40] also revealed that calcification develops regularly from the cusps to the leaflet free edge. The same patterns have also reported in [41, 42]. In this study, we are not aiming to study patient-specific AV dynamics, but to focus on the effect of calcification-induced stenosis on AV dynamics in an idealized AV model. Figure 1(b) shows a schematic representation of different calcification burden studied in this study. In detail, each AV leaflet is divided into a calcified region (the grey color) near the aortic root (cusp) and a healthy non-calcified zone (the red color) towards the free edge. Note, the calcified region connects to the healthy region directly without overlapping. The progression of calcification in each leaflet is characterized by varying the size of the calcified zone. The initial site of calcification is defined at the regions with high flexure that is the attachment of the cusps to the aortic wall [43]. We have designed three CAVS cases according to the ratio of calcification area in relation to the total leaflet area, they are CAVS1: 20%, CAVS2: 30%, and CAVS: 40%, see Figure 1(b). We also include a healthy AV case (HAV) with 0% calcification for comparison.
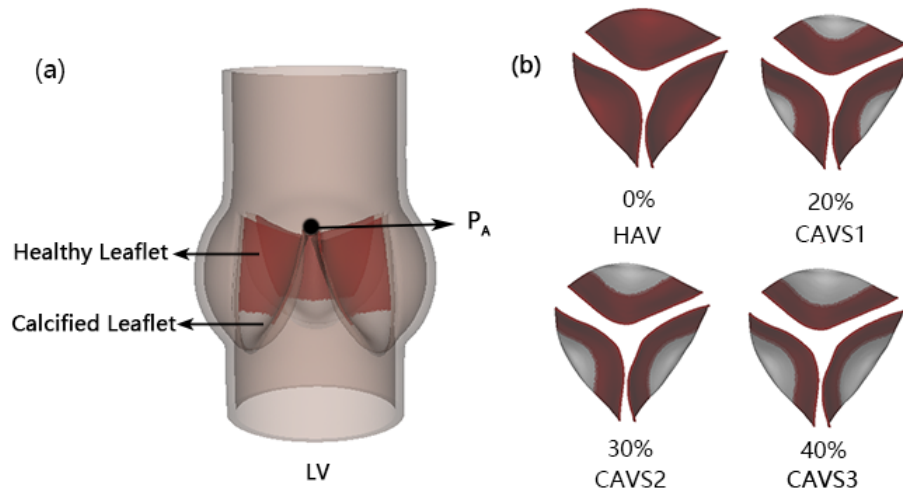
Figure 1. (a) The AV model mounted in a straight tube; (b) Schematic diagrams of different calcification burden described by the ratio between the calcified area and the total leaflet area.

The constitutive equations, parameters, and fibre orientations of the AV leaflets are based on the results from [34]. In specific, the constitutive function for the leaflets is

$$W_1 = C_{10} \left(e^{C_{01}(I_1 - 3)} - 1 \right) + \frac{k_1}{2k_2} \left[e^{k_2(I_4 - 1)^2} - 1 \right], \tag{2.1}$$

in which C_{10}, C_{01}, k_1, k_2 are constitutive parameters, $I_1 = \text{tr}(\mathbb{F}^T\mathbb{F})$ with $\mathbb{F}$ the deformation gradient, $I_4 = \mathbf{f}_0 \cdot (\mathbb{F}^T\mathbb{F}\mathbf{f}_0)$ with $\mathbf{f}_0$ the fibre direction in the reference state. Parameter values can be found in Table 1. The calcification deposits is described by an incompressible Neo-Hookean model,

$$W_2 = \frac{\alpha}{2}(I_1 - 3), \tag{2.2}$$

where α is the shear modulus, D_1 is the bulk modulus, $J = \det(\mathbb{F})$. Considering the Poisson's ratio (v) of 0.3 and the Young's modulus (E) of 20 MPa for the calcification [11, 12], then we have $\alpha = E/2(1 + v)$. The first Piola-Kirchhoff stress tensors ($\mathbb{P}$) for healthy leaflet and the calcification deposit are

$$\mathbb{P}^{W1} = 2C_{10}C_{01}e^{C_{01}(I_1-3)}\mathbb{F} + 2k_1(I_4 - 1)e^{k_2(I_4-1)^2}\mathbb{F}\mathbf{f}_0 \otimes \mathbf{f}_0 - p_0\mathbb{F}^{-T}, \tag{2.3}$$

$$\mathbb{P}^{W2} = \alpha\mathbb{F} - p_1\mathbb{F}^{-T}, \tag{2.4}$$

in which p_0 and p_1 are Lagrange multipliers to enforce incompressibility. Note both the healthy leaflets and calcification are assumed to be incompressible in this study.

Table 1. Constitutive parameter values adapted from [34], and α is obtained from [11].

C_{10}(kPa)	C_{01}	k_1(kPa)	k_2	α (MPa)
1.21	7.99	24.23	57.62	7.69

2.2. The IB/FE model

The IB/FE method [28, 30] uses finite element discretization for solids and finite difference discretization for fluids. In brief, let $\mathbf{X} = (X_1, X_2, X_3) \in U \subset R^3$ denote Lagrangian material coordinates, and let $\mathbf{x} = (x_1, x_2, x_3) \in \Omega \subset R^3$ represent Eulerian coordinates. The mutual conversion between them is realized by the integral transformation of the Delta function $\delta(\cdot)$, and $\chi(\mathbf{X}, t) \in \Omega$ denotes the physical position of the structure point $\mathbf{X}$ at time t. The governing equations of the IB/FE system are

$$\rho \left(\frac{\partial \mathbf{u}}{\partial t}(\mathbf{x}, t) + \mathbf{u}(\mathbf{x}, t) \cdot \nabla \mathbf{u}(\mathbf{x}, t) \right) = -\nabla p(\mathbf{x}, t) + \mu \nabla^2 \mathbf{u}(\mathbf{x}, t) + \mathbf{f}(\mathbf{x}, t), \tag{2.5}$$

$$\nabla \cdot \mathbf{u}(\mathbf{x}, t) = 0, \tag{2.6}$$

$$\mathbf{f}(\mathbf{x}, t) = \int_\Omega \mathbf{F}(\mathbf{X}, t) \delta(\mathbf{x} - \chi(\mathbf{X}, t)) \, d\mathbf{X}, \tag{2.7}$$

$$\frac{\partial \chi}{\partial t}(\mathbf{X}, t) = \int_\Omega \mathbf{u}(\mathbf{x}, t) \delta(\mathbf{x} - \chi(\mathbf{X}, t)) \, d\mathbf{x}, \tag{2.8}$$

$$\int_U \mathbf{F}(\mathbf{X}, t) \cdot \mathbf{V}(\mathbf{X}) \, d\mathbf{X} = -\int_U \mathbb{P}^e(\mathbf{X}, t) : \nabla_\mathbf{X} \mathbf{V}(\mathbf{X}) \, d\mathbf{X}, \tag{2.9}$$

where $\rho = 1.0 \, \text{g/ml}$ is blood density, $\mu = 4 \, \text{cP}$ is blood viscosity. Because the inner radius of the aortic tube is 1.3 cm, the accumulation of red blood cells can be ignored in our model [44], thus in this study, the blood is regarded as a Newtonian fluid, a widely adopted assumption when modelling blood flow in large arteries [45]. The velocity field $\mathbf{u}(\mathbf{x}, t)$ is in Eulerian form, $p(\mathbf{x}, t)$ is the Eulerian pressure field, $\mathbf{f}(\mathbf{x}, t)$ is the Eulerian elastic force density, and $\mathbb{P}^e$ is the first Piola-Kirchhoff stress tensor that can be derived from selected strain energy functions, see Section 2.1 for details. Further details about the IB/FE framework and its application in soft tissue can be found in [28, 30, 31] and its validation in [46, 47].
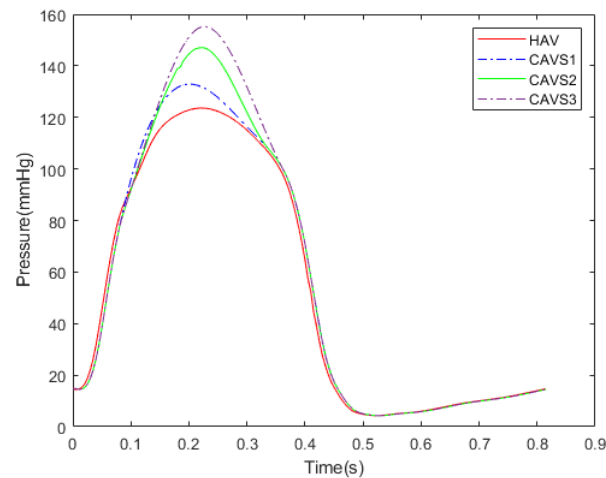
2.3. The Windkessel model

For the healthy case HAV, a physiological LV pressure profile is applied to the inlet with a peak value of 120 mmHg as shown in Figure 2. With increased calcification burden, the AV will impose higher resistance for the transvalvular flow, thus a higher systolic pressure is used for CAVS cases. LV pressure profiles for CAVS cases can also be found in Figure 2 which are based on literature reported data [15]. In general, the higher the calcification burden, the higher the systolic LV pressure.

In the outlet, the aortic pressure is maintained at a range of 120/80 mmHg using a three-element Windkessel model due to the Baroreflex mechanism [48]. In brief, the three-element Windkessel model reads

$$C \frac{dP_\text{Wk}}{dt} + \frac{P_\text{Wk}}{R_\text{p}} = Q_\text{Ao}, \tag{2.10}$$

$$P_\text{Ao} = Q_\text{Ao} R_\text{c} + P_\text{Wk}, \tag{2.11}$$

where R_c is the characteristic resistance, R_p represents the peripheral resistance and C is the arterial compliance. P_{WK} is the pressure stored in the Windkessel model. Details of the three-element Windkessel model can be found in [26], and parameter values are listed in Table 2.

Figure 2. LV pressure profiles for all studied cases derived from literature reported data [15].

Table 2. Parameter values of the Windkessel model, adapted from [49].

R_C (mmHg ml^{-1}s)	R_P (mmHg ml^{-1}s)	C (ml mmHg^{-1})
0.033	0.79	1.75

3. Numerical implementation

The whole model is immersed in a fluid region of 8 cm × 8 cm × 13 cm that is discretized into a regular 80 × 80 × 128 Cartesian grids. The grid size is the same as in our previous work for simulating the mitral valve dynamics in a straight tube [28], in which a grid convergence study was performed. Thus, in this study, we adopt a similar spatial spacing with $\Delta x_1 = \Delta x_2 = 0.1$ cm and $\Delta x_3 = 0.1016$ cm as in [28]. Figure 3 shows the meshes of the aortic tube and the aortic valve used in this study. The AV leaflet is meshed with very fine tetrahedral elements because of the very thin leaflet thickness (0.04 cm), the outer tube covering the AV is meshed with a dense mesh while the remaining tube is meshed with coarse hexahedral elements. Note the mesh density of the outer tube is not critical since the outer tube is fixed throughout the simulation, and its mechanical deformation is not computed but to prevent blood leakage across the tube wall. In sum, the solid region is subdivided into 196,028 elements. Prescribed LV pressure profiles (Figure 2) are used for each CAVS at the inlet (the LV side). Meanwhile, the Windkessel model is used to provide the physiologically accurate aortic pressure in the outlet. The whole aortic tube is fixed with zero displacements and the environmental flow outside the aortic tube is free to flow with 0 pressure on all boundaries of the computational domain. Details of the boundary conditions can also be found in [34].

We set the cardiac cycle to be 0.8 s and the time step size 5e-6 s following our previous study [28]. The very small time step is because of the explicit time-stepping scheme. Details of the spatial and temporal discretization can be found in [28, 30]. The periodic convergence test has been carried out in [34] using the HAV model, which has shown that this FSI AV model can reach periodic convergence from the second period and the effective opening area, left ventricular energy loss, stress, and others are all consistent with the reference data. Considering the computational time for one cardiac cycle

requires several days, thus in this study, only first two cardiac cycles are simulated and the results from the second cycle are analyzed. The IB/FE AV model is implemented using the IBAMR software infrastructure (https://github.com/IBAMR/IBAMR). In this study, the Cartesian computational domain is further discretized with 2 nested grid levels with a refinement ratio of 4 between the two levels for improved computational efficiency. Note the structural mesh is not refined during the simulation.
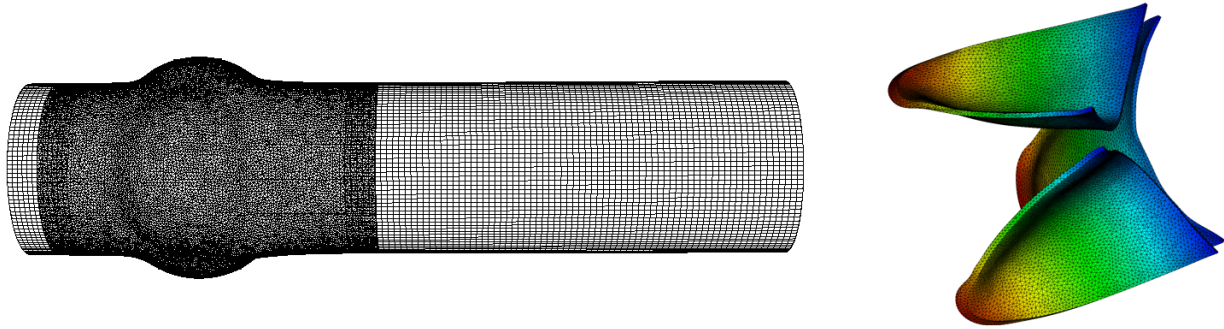
Figure 3. Meshes of the aortic tube (left) and the aortic valve (right) colored by its z-coordinate.

4. The hemodynamic parameters

To evaluate valvular performance, the following hemodynamic parameters are introduced, including the regurgitant fraction (RF), the mean transvalvular pressure gradient (TPG), the effective orifice area (EOA), the performance index (PI), and the energy loss (EL) of the LV.

The regurgitant fraction (RF) reflects the volume ratio of the regurgitant blood into LV through AV. It is defined as [50]

$$\text{RF} = (V_R + V_L)/V_F, \tag{4.1}$$

in which V_F is the forward volume, V_R is the regurgitant volume, and V_L is the leakage volume.

The mean transvalvular pressure gradient (TPG) measures the potential energy loss. It is the average pressure gradient across the AV in systole,

$$\text{TPG} = \frac{1}{T} \int_T (P_{\text{LV}} - P_{\text{AO}}) dt, \tag{4.2}$$

where P_{LV} and P_{AO} are the pressures at LV and aortic sides, and T is the systolic duration.

The effective orifice area (EOA) [50] is related to the degree of obstruction of blood flow,

$$\text{EOA} = \frac{Q_{\text{rms}}}{51.6\sqrt{TPG/\rho}}, \tag{4.3}$$

$$Q_{\text{rms}} = \left(\frac{1}{T} \int_T Q(t)^2 dt \right)^{1/2}, \tag{4.4}$$

in which $Q(t)$ is the flow rate, and Q_{rms} represents the root mean square volumetric flow rate.

Performance index (PI) [51] provides the normalized resistance of valve using a size-independent method,

$$\text{PI} = \frac{\text{EOA}}{A_{\text{sew}}}, \tag{4.5}$$

in which A_{sew} is the valve sewing ring area.

The energy loss of LV (EL) is calculated as [39]

$$\text{E}_{\text{L}} = 0.1333 \int_{t_1}^{t_2} \Delta p(t) Q(t) dt, \tag{4.6}$$

in which t_2-t_1 denote the duration of one cardiac cycle, and $\Delta p = P_{\text{Ao}} - P_{\text{LV}}$.

5. Results

5.1. Displacement fields

Figure 4 shows the motion of the AV with different calcification degrees in the opening stage ($t = 0.12$ s, $t = 0.18$ s) and the closing stage ($t = 0.36$ s, $t = 0.39$ s, $t = 0.47$ s), respectively. It can be seen that the displacements in the calcified area are small, which is in line with the severity of calcification.
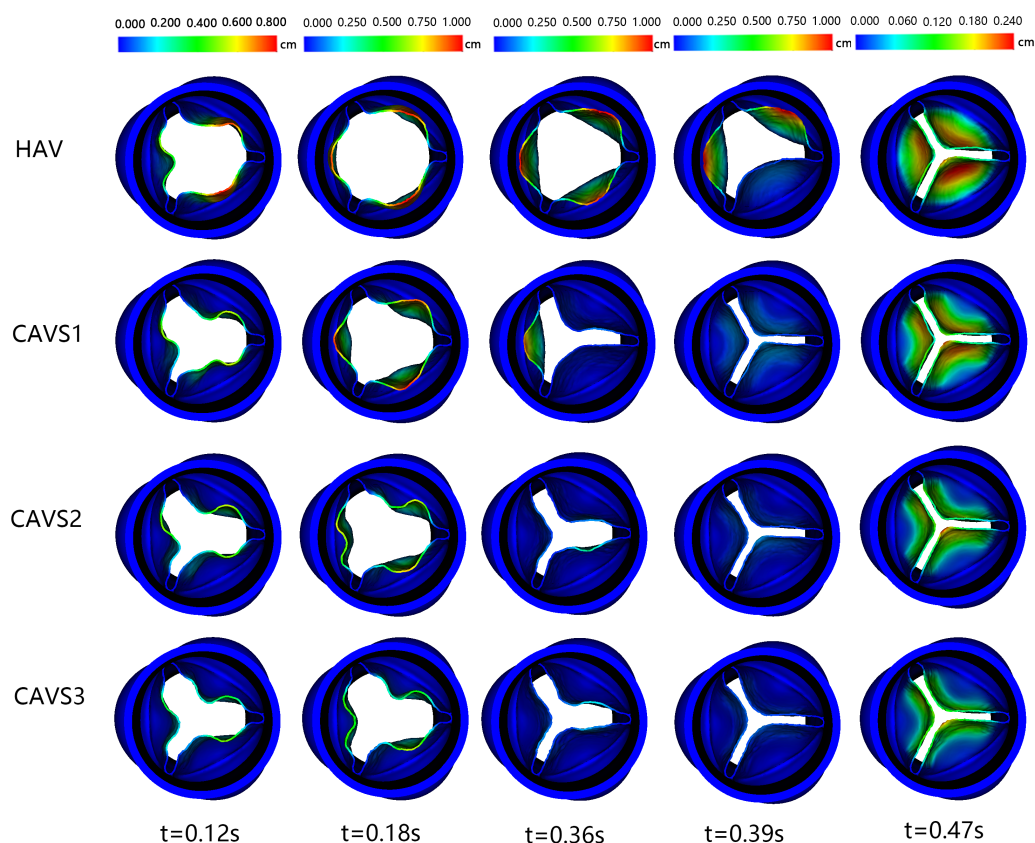
Figure 4. Movements of AV leaflets at different time.

With the progress of CAVS, the on-off state of AV has changed dramatically. In the initial stage, the AV gradually opens and the HAV reaches a larger opening orifice than CAVS1, CAVS2, and CAVS3. The three calcified valves all reach their maximum opening area when $t = 0.18s$. While the orifice area decreased dramatically in calcified AV, from 3.55 cm^2 in a healthy state to 1.41 cm^2 in moderate stenosis (CAVS3) at $t = 0.18$ s. Thus, during the opening phase, local stiffness of the valve due to calcification results slow opening with a small orifice. In the closing period, at $t = 0.36$ s and $t = 0.39$ s, the opening of the HAV is still relatively large in the early stage of the closure period. However, CAVS1, CAVS2, and CAVS3 have almost been closed, the average and maximum displacements are reduced to half of HAV. When $t = 0.47$ s, all AVs are closed. The valve cusp of calcified cases does not move much compared to the other areas due to the calcification, while the free edge of the valve leaflet is still healthy, and thus it can open and close freely in all cases. For this reason, the maximum displacement usually locates at the free edge, but decreases as the degree of calcification increases. From Figure 4, we can expect that calcification can lead to a decrease in cardiac output and result in an insufficient blood supply due to small opening orifice.

Table 3. Spatial average and maximum displacements at different time.

Cases	Average displacement (cm)				Maximum displacement (cm)			
	0.18 s	0.36 s	0.39 s	0.47 s	0.18 s	0.36 s	0.39 s	0.47 s
HAV	0.041	0.031	0.023	0.017	0.994	1.016	1.037	0.246
CAVS1	0.026	0.014	0.015	0.015	0.952	0.881	0.179	0.224
CAVS2	0.021	0.013	0.013	0.014	0.788	0.359	0.182	0.233
CAVS3	0.018	0.012	0.011	0.013	0.685	0.239	0.132	0.222

It can be seen from Table 3 that the average and the maximum displacements decrease with the increase of the calcification severity. In sum, calcification can have an adverse effect on the mobility of the valve.

We further divide the cardiac cycle into the opening, fully-opened and closing phases. The opening phase represents the duration of the AV from the beginning of opening to the fully opened state. Fully-opened phases is the duration for which the maximum orifice area is maintained. The closing phase represents the duration from pre-closed to fully-closed states. The opening time for the four cases is similar that is around 0.1 s. While calcification can affect the duration of AV in the full-opened phase as summarized in Table 4. During the fully-opened phase, the duration is reduced from 0.15 s in the healthy case to 0.1 s in the calcified AVs. Therefore, the calcified valve not only has a small opening orifice but also has a short duration of the fully-opened phase. In the closing phase, the duration of the calcified valve is slightly longer than that of HAV, this increasing trend is consistent with [12].

Table 4. The duration of AV opening, fully-opened and closing phases.

| Cases	Fully-opened (s)	Closing (s)
HAV	0.15	0.15
CAVS1	0.10	0.155
CAVS2	0.11	0.16
CAVS3	0.10	0.16

5.2. *Transvalvular flow fields*

Figure 5 shows the velocity field across the AV at the opening phase ($t = 0.12$ s, $t = 0.2$ s) and the closing phase ($t = 0.3$ s, $t = 0.35$ s, $t = 0.41$ s). In the opening phase, the pressure of the left ventricle is higher than that on the aortic side, and the blood flows into the aortic side. Due to the different calcification areas of the four models, the blood flow is also different. When $t = 0.2$ s, the AV is fully opened. Because of the obstruction of valve opening in calcified AVs, different forward jets are formed, and the maximum flow velocity gradually increases with increased calcification area. In particular, the maximum flow velocity of CAVS3 exceeds 3 m/s. In the closing phase ($t = 0.3$ s), the blood enters into the aorta with a more homogeneous velocity field compared to the calcified cases, in which the jets are still maintained. At $t = 0.41$ s, the HAV shows clear regurgitant flow, and the volume is 5.05 mL, while the calcified valves are completely closed at this time and no clear regurgitation flow can be seen.
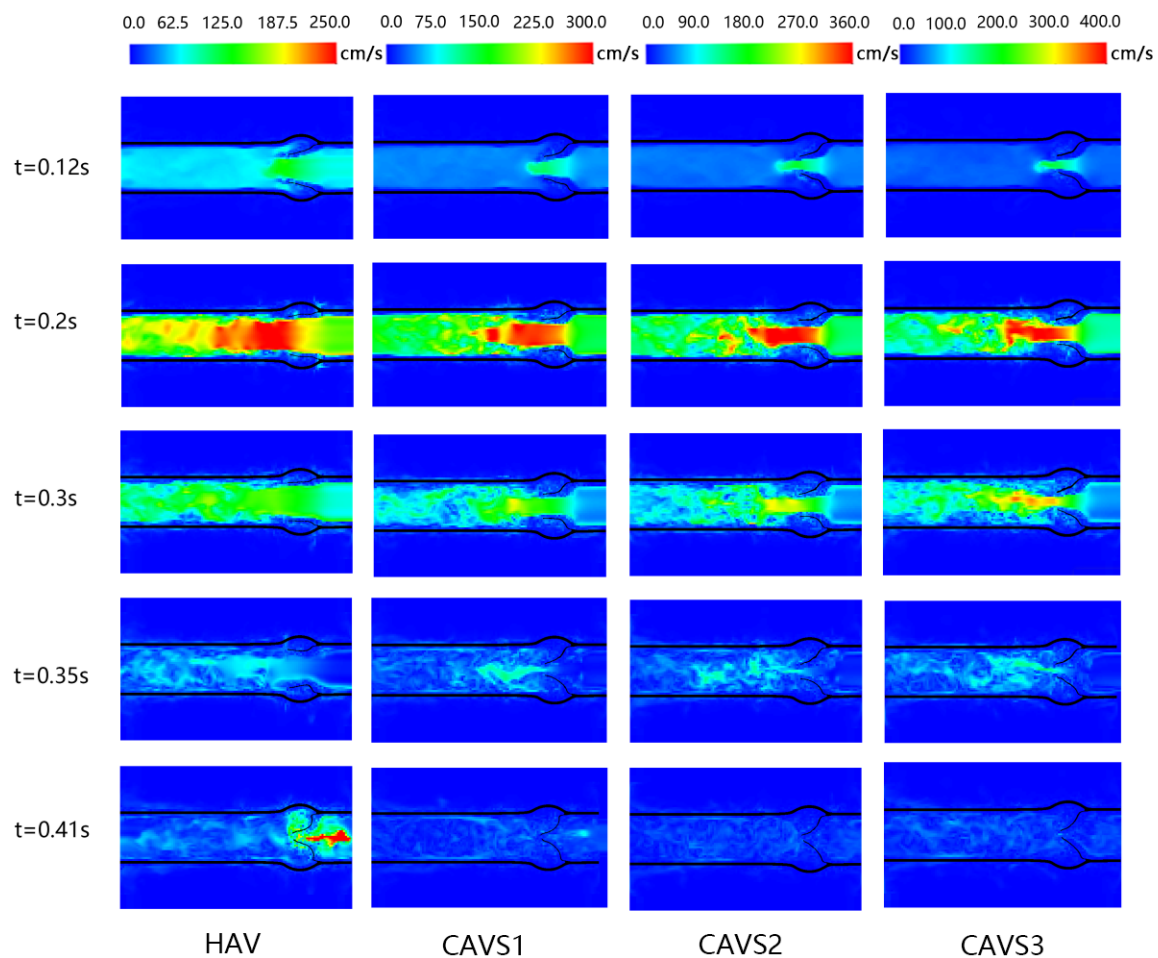

Figure 5. The fluid velocity fields in different cases.

Figure 6 shows the velocity profiles at the location P_A as defined in Figure 1. As the calcified area increases, the peak velocity also increases from 2.27 m/s for HAV to 3.98 m/s for CAVS3. During the closure period of the AV, the HAV shows larger velocity oscillations, while the amplitude decreases as

the calcification area increases. Those oscillations correspond to the closure regurgitant flow.
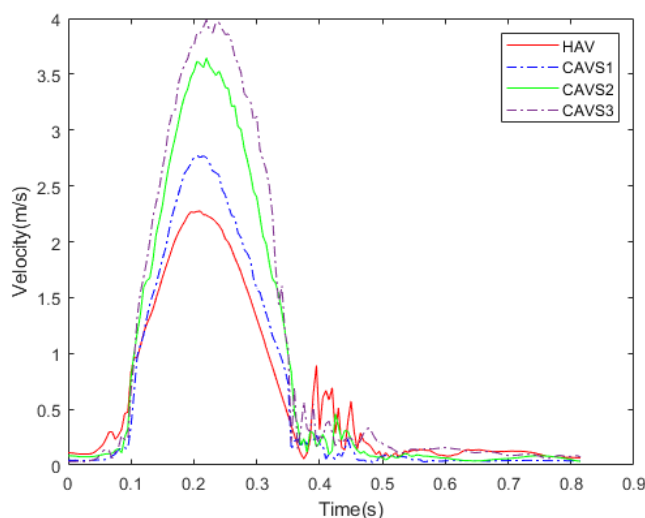
Figure 6. The velocity profiles at the location P_A defined in Figure 1.
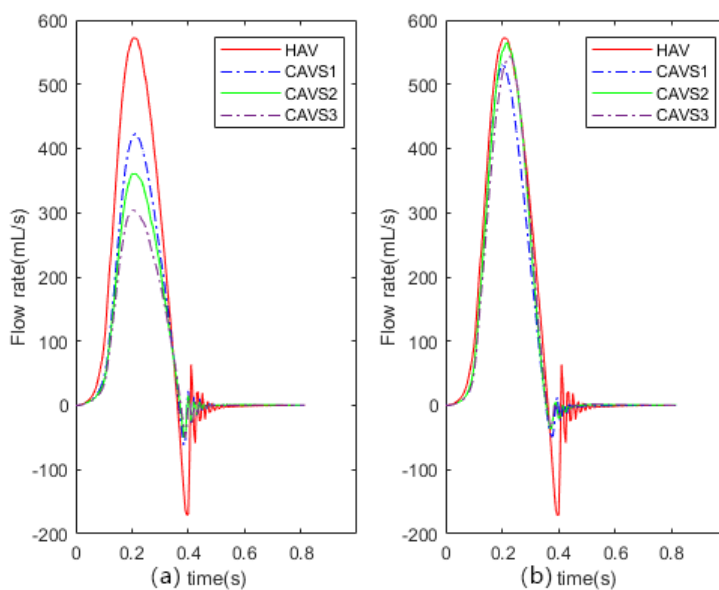

Figure 7. Flow rates across the AV in one cardiac cycle without (a) and with (b) cardiomodulation.

Figure 7(a) shows the flow rates through the AVs over a cardiac cycle without maintaining the aortic pressure at 120/80 mmHg. It can be found that the peak flow rate gradually decreases from 571.34 to 302.82 mL/s with the increased calcified severity. The forward flow volume is reduced from 97.21 mL for HAV to 69.66 mL for CAVS1, 61.23 mL for CAVS2, and 53.24 mL for CAVS3. During the closing phase, the maximum regurgitant flow rate of HAV is 170.57 mL/s, much higher than those of calcified

AV (around 50 mL/s). Figure 7(b) shows the flow rates through the AV when maintaining the aortic pressure at 120/80 mmHg. It can be found that the flow of calcified AV is much closer to the flow rate of HAV compared to Figure 7(a).

5.3. Strain and stress analysis

The fibre strain distributions of the AV in the fully-opened, pre-closed (the AV leaflets start to close), and fully-closed states are shown in Figure 8. It can be observed that the strain distribution of the calcification model is significantly different from that of HAV. In particular, CAVS2 and CAVS3 experience a large squeezed region in the centre region of the valve, which is not present in HAV at $t = 0.24$ s when the AV is fully opened. Meanwhile, it can be found that the strain forms a distinct boundary between calcified and healthy regions. Low strains are seen in the calcified regions, while high strains are usually concentrated at this boundary. Arazani et al. [17] have suggested that a compliance mismatch occurring in this region may lead to a local increase in strain, which leads to further calcium deposition and propagation of calcification. The reduction in strain in the calcified region throughout the cardiac cycle could be explained by calcium depositions that increase leaflet stiffness. At $t = 0.48$ s, the leaflet strain reaches the largest. The peak strains in Figure 8 are consistent with the range reported in [14] with the maximum magnitude greater than 0.1.
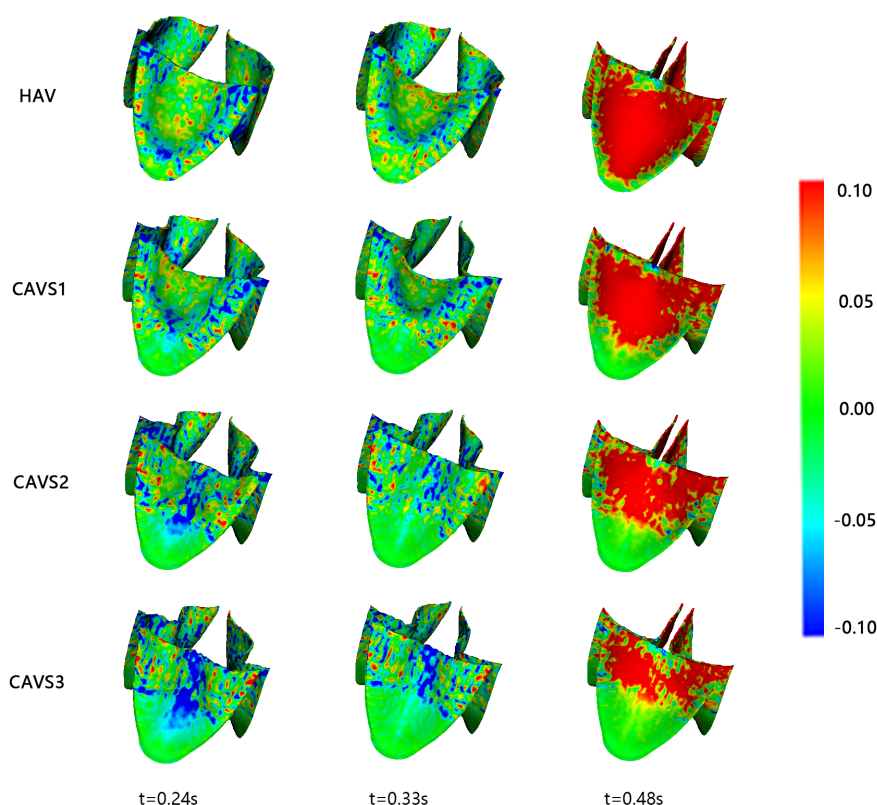
Figure 8. Fibre strain (unitless) distributions of AV in fully open (0.24 s), pre-closed (0.33 s) and fully closed (0.48 s) phases.

Figure 9 presents the fibre stress of the valve at 0.24 s and 0.48 s. As calcification develops, locations of high mechanical stress appear and concentrate in commissures at the fully-opened state. When severe calcification is present, it gradually extends to the base of the valve. The magnitude of the stress in the belly region in the closing phase is much larger than the corresponding magnitude in the opening phase. The high stress regions mostly concentrate in the non-calcified regions, while all cases are experiencing very high fibre stresses at the closing phase. The distribution and magnitude of stress of all cases are in general agreement with [52, 53] within a range of < 500 kPa. Thus, calcified valves experience a local increase in stress and strain, which in turn promotes the further progression of calcification.
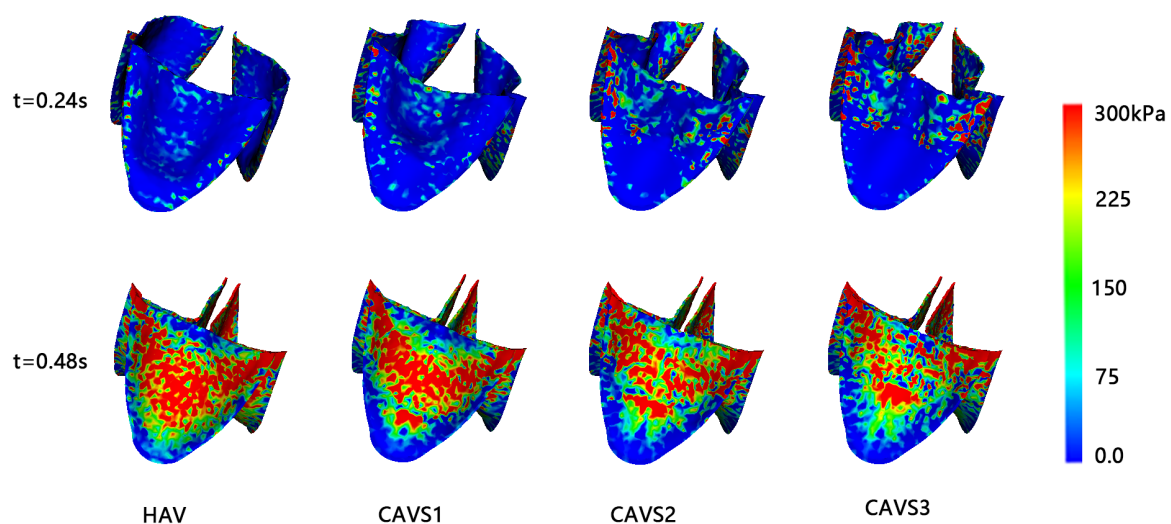
Figure 9. Fibre stress distributions of AV in fully-opened (0.24 s) and fully-opened (0.48 s) phases.

5.4. Hemodynamic performance

To analyze the effect of calcification on AV hemodynamic parameters, the results of V_F, V_R, V_L, RF, PI, EL, the maximum velocity, EOA and TPG are summarized in Tables 5 and 6. In general, V_F, V_R, V_L, and RF values in CAVS are lower than those of HAV, while TPG and EL increase significantly with increased calcification areas. EOA and PI are the most intuitive indices of the severity of calcification-induced stenosis and are negatively correlated with calcification severity. Since the degree of stenosis can be reflected by the maximum flow velocity, TPG, and EOA, we further include literature reported values [15, 19, 54–58] in Table 6, based on which we could classify each CAVS case with a medical grade of AV stenosis. It can be found that the results from our models agree well with the clinical classification except that the maximum velocity is slightly higher than in vivo reference data.

Table 5. The summary of hemodynamic parameters V_F, V_R, V_L, RF, PI, and EL.

Cases	V_F (mL)	V_R (mL)	V_L (mL)	RF (%)	PI	EL (mJ)
HAV	97.21	5.05	1.03	6.25	0.67	109.44
CAVS1	80.58	1.25	0.27	1.88	0.43	135.82
CAVS2	88.39	0.88	0.12	1.13	0.33	281.86
CAVS3	85.29	0.78	0.06	0.98	0.27	361.91

Table 6. Model predicted results compared to literature reported clinical data [15, 19, 54–58] on the classification of AV stenosis including the maximum velocity, EOA and TPG.

	Maximum velocity (m/s)		EOA (cm^2)		TPG (mmHg)	
	in-vivo	model	in-vivo	model	in-vivo	model
healthy	< 2	2.27	3.9 ± 1.2	3.55	< 5	4.34
sclerosis	< 2	2.77	3.9 ± 1.2	2.26		7.80
Mild stenosis	2–2.9	3.65	> 1.5	1.73	< 20	16.28
Moderate stenosis	3–3.9	3.98	1–1.5	1.41	20–39	22.79

6. Discussion

In this paper, by using the IB/FE method, we have studied AV dynamics with increased calcification. The initial location of calcification is at the valve cusp and gradually spreads radially to the free edge. One healthy model and three diseased models are constructed using the ratio of the area occupied by calcification. Among them, the hyperelastic constitutive equation that best describes the valve mechanical behaviour in previous studies [34] is used for healthy valves, and an isotropic Neo-Hookean model is used for calcification. For fluid boundary conditions, different LV pressures are assigned for each CAVS by maintaining the aortic pressure at 120/80 mmHg. A classic Winkessel model is further used to provide the outlet boundary condition at the aortic side. Compared with the vascular tree model [59], although the Windkessel cannot simulate the pulse wave transmission, it is simple and easy to implement to provide an accurate physiological pressure for the outlet. The same practice can also be seen in [15]. To assess the effect of calcification on AV performance, we analyzed AV displacement fields, transvalvular flow fields, strain, stress and hemodynamic performance. Our results show that calcification can a significant effect on the dynamics of AV.

As can be seen from Table 5, with the increase of calcification area, V_F, V_R, V_L, and RF all show a decreasing trend. V_F of HAV is 97.21 mL that is higher than the values from calcified cases (about 80 mL). Calcified leaflets connected to the aortic wall result a decrease in the volume of blood which returns from the aorta to the LV, while V_R and V_L decrease drastically with the increase of calcification area, which is also reflected in Figures 4 and 5.

TPG is one of the important indicators to assess valve stenosis. In this study, TPG increases with calcification from 4.34 mmHg in HAV to 22.79 mmHg in CAVS3, which is 5-fold higher than HAV. Increased TPG can have an significant impact on valve performance and drive compensatory LV hypertrophy to accommodate increased after-load [60]. A larger EOA corresponds to a smaller pressure drop, resulting in less energy loss. With the development of calcification, the opening area in CAVS3

decrease to less than half of the healthy state, which can also be seen from Figure 4. PI shows how well the valve design utilizes its total installed area and is inversely proportional to the calcified area. As can be seen from the Figure 5, the calcified valve results in a orifice diameter decreased from 2.2 cm for HAV to 1.6 cm for CAVS1, and to 1.45 cm for CAVS2, and to 1.35 cm for CAVS3 as shown in Figure 5. The valve orifice ratios relative to HAV are 75, 61 and 43% of HAV, respectively. As discussed previously, larger TPG usually corresponds to larger EL. The EL of HAV is 109.44 mJ, which is very close to the reference value (129.03 mJ) reported in [50]. However, the EL of CAVS3 with moderate stenosis is 361.91 mJ, which is much larger than HAV.

For the evaluation of various performance indicators of HAV, readers refer to our previous study [34]. For CAVS1, the maximum velocity is 2.77 m/s, the opening area is 2.26 cm^2, and the transvalvular pressure difference is 7.80 mmHg, which is in line with the clinical diagnosis of sclerosis as shown in Table 6. EOA and TPG of CAVS2 agree with the range of mild stenosis. For CAVS3, the maximum velocity, TPG, and EOA are consistent with moderate stenosis. Therefore, the selected three calcification models in this study represent typical clinical cases from sclerosis to mild stenosis and to moderate stenosis.

Although the simulated results agree well the reported clinical data [15, 19, 54–58], limitations exist in this study. For example, we have not considered the pattern of calcification, but assumed to be uniformly distributed over the leaflets and follow a idealized growth pattern from the cusp to the free edge. The thickness of the valve is not uniform but increases with age due to the deformation of collagen fibres and calcium accumulation. For example, Weinberg et al. [61] studied AV aging from 20 to 80 years by including tissue flexibility degradation, thickening and calcification with aging. It is challenging to calculate wall shear stress in our IB/FE based AV model because the fluid mesh and the solid mesh are not body-fitted but overlapped. Thus future development in reconstructing accurate wall shear stress from IB/FE predicted velocity filed is needed, for example by including a boundary layer since wall shear stress is highly sensitive to the fluid mesh quality [62]. Furthermore, the blood is considered to be Newtonian with laminar flow assumption, future studies shall also investigate how non-Newtonian model affects AV dynamics, especially in stenotic AV when the turbulence is present [63], the damage to blood cells [64], and the impact on calcification progression [17]. Last but not the least, the constitutive model of calcification is simple without considering its complex structures, a microstructure-informed biomechanical model of calcification will be needed for a patient-specific simulation [65].

7. Conclusions

In this work, we have studied the effect of calcification on human aortic dynamics. By using the IB/FE method, FSI simulations of AV dynamics are performed for healthy and three calcification cases characterized by increased calcified area in the leaflets. Our results show that calcification can significantly affect AV function and the selected calcified cases are able to describe the progression of calcification. In specific, calcified AVs have smaller opening area and higher forward jet flow. The higher the degree of calcification, the heavier the ventricular loading, resulting in a significant increase in left ventricular energy loss and transvalvular pressure gradient. Moreover, calcified valves could cause an increase in local stress and strain, which in turn promotes the development of calcification. This further suggests that the presence of calcification could lead to a vicious circle and should be

treated at the right time. The maximum velocity, EOA and TPG predicted by our models are in general consistent with the clinical stenosis classification. It is expected that the IB/FE FSI simulated AV model has the potential to deepen the understanding of AV stenosis-induced ventricular dysfunction and facilitate the development of computational engineering-assisted medical diagnosis in AV-related diseases.

Acknowledgments

Conflict of interest

On behalf of all authors, the corresponding author states that there is no conflict of interest.

References

1. G. W. Eveborn, H. Schirmer, G. Heggelund, P. Lunde, K. Rasmussen, The evolving epidemiology of valvular aortic stenosis, the tromsø study, *Heart*, **99** (2013), 396–400. http://dx.doi.org/10.1136/heartjnl-2012-302265

2. W. Pan, D. Zhou, L. Cheng, X. Shu, J. Ge, Candidates for transcatheter aortic valve implantation may be fewer in China, *Int. J. Cardiol.*, **168** (2013), e133–e134. https://doi.org/10.1016/j.ijcard.2013.08.028

3. W. D. Edwards, The changing spectrum of valvular heart disease pathology, in *Harrison's Advances in Cardiology*, (2002), 317–323.

4. B. F. Stewart, D. Siscovick, B. K. Lind, J. M. Gardin, J. S. Gottdiener, V. E. Smith, et al., Clinical factors associated with calcific aortic valve disease, *J. Am. Coll. Cardiol.*, **29** (1997), 630–634. https://doi.org/10.1016/S0735-1097(96)00563-3

5. A. G. Kidane, G. Burriesci, P. Cornejo, A. Dooley, S. Sarkar, P. Bonhoeffer, et al., Current developments and future prospects for heart valve replacement therapy, *J. Biomed. Mater. Res. Part B*, **88B** (2009), 290–303. https://doi.org/10.1002/jbm.b.31151

6. S. J. Head, M. Çelik, A. P. Kappetein, Mechanical versus bioprosthetic aortic valve replacement, *Eur. Heart J.*, **38** (2017), 2183–2191. https://doi.org/10.1093/eurheartj/ehx141

7. F. J. Schoen, R. J. Levy, Calcification of tissue heart valve substitutes: progress toward understanding and prevention, *Ann. Thorac. Surg.*, **79** (2005), 1072–1080. https://doi.org/10.1016/j.athoracsur.2004.06.033

8. M. Ruel, A. Kulik, B. K. Lam, F. D. Rubens, P. J. Hendry, R. G. Masters, et al., Long-term outcomes of valve replacement with modern prostheses in young adults, *Eur. J. Cardio-Thorac. Surg.*, **27** (2005), 425–433. https://doi.org/10.1016/j.ejcts.2004.12.002

9. J. G. Mönckeberg, Der normale histologische bau und die sklerose der aortenklappen, *Virchows Arch. path Anat.*, **176** (1904), 472–514. https://doi.org/10.1007/BF02041318

10. G. Novo, G. Fazio, C. Visconti, P. Carità, E. Maira, K. Fattouch, et al., Atherosclerosis, degenerative aortic stenosis and statins, *Curr. Drug Targets*, **12** (2011), 115–121. https://doi.org/10.2174/138945011793591545

11. O. Mutlu, H. E. Salman, H. C. Yalcin, A. B. Olcay, Fluid flow characteristics of healthy and calcified aortic valves using three-dimensional lagrangian coherent structures analysis, *Fluids*, **6** (2021), 203. https://doi.org/10.3390/fluids6060203

12. A. R. Kivi, N. Sedaghatizadeh, B. S. Cazzolato, A. C. Zander, R. R. Thomson, A. J. Nelson, et al., Fluid structure interaction modelling of aortic valve stenosis: effects of valve calcification on coronary artery flow and aortic root hemodynamics, *Comput. Methods Programs Biomed.*, **196** (2020), 105647. https://doi.org/10.1016/j.cmpb.2020.105647

13. G. Luraghi, F. Migliavacca, C. Chiastra, A. Rossi, B. Reimers, G. G. Stefanini, et al., Does clinical data quality affect fluid-structure interaction simulations of patient-specific stenotic aortic valve models? *J. Biomech.*, **94** (2019), 202–210. https://doi.org/10.1016/j.jbiomech.2019.07.047

14. R. Halevi, A. Hamdan, G. Marom, M. Mega, E. Raanani, R. Haj-Ali, Progressive aortic valve calcification: three-dimensional visualization and biomechanical analysis, *J. Biomech.*, **48** (2015), 489–497. https://doi.org/10.1016/j.jbiomech.2014.12.004

15. R. Halevi, A. Hamdan, G. Marom, K. Lavon, S. Ben-Zekry, E. Raanani, et al., Fluid–structure interaction modeling of calcific aortic valve disease using patient-specific three-dimensional calcification scans, *Med. Biol. Eng. Comput.*, **54** (2016), 1683–1694. https://doi.org/10.1007/s11517-016-1458-0

16. H. Maleki, S. Shahriari, L. G. Durand, M. R. Labrosse, L. Kadem, A metric for the stiffness of calcified aortic valves using a combined computational and experimental approach, *Med. Biol. Eng. Comput.*, **52** (2014), 1–8. https://doi.org/10.1007/s11517-013-1113-y

17. A. Arzani, M. R. K. Mofrad, A strain-based finite element model for calcification progression in aortic valves, *J. Biomech.*, **65** (2017), 216–220. https://doi.org/10.1016/j.jbiomech.2017.10.014

18. V. Meschini, F. Viola, R. Verzicco, Modeling mitral valve stenosis: a parametric study on the stenosis severity level, *J. Biomech.*, **84** (2019), 218–226. https://doi.org/10.1016/j.jbiomech.2019.01.002

19. F. Viola, V. Meschini, R. Verzicco, Effects of stenotic aortic valve on the left heart hemodynamics: a fluid-structure-electrophysiology approach, preprient, arXiv:2103.14680.

20. F. Viscardi, C. Vergara, L. Antiga, S. Merelli, A. Veneziani, G. Puppini, et al., Comparative finite element model analysis of ascending aortic flow in bicuspid and tricuspid aortic valve, *Artif. Organs*, **34** (2010), 1114–1120. https://doi.org/10.1111/j.1525-1594.2009.00989.x

21. F. Sturla, M. Ronzoni, M. Vitali, A. Dimasi, R. Vismara, G. Preston-Maher, et al., Impact of different aortic valve calcification patterns on the outcome of transcatheter aortic valve implantation: a finite element study, *J. Biomech.*, **49** (2016), 2520–2530. https://doi.org/10.1016/j.jbiomech.2016.03.036

22. J. Donea, S. Giuliani, J. P. Halleux, An arbitrary lagrangian-eulerian finite element method for transient dynamic fluid-structure interactions, *Comput. Methods Appl. Mech. Eng.*, **33** (1982), 689–723. https://doi.org/10.1016/0045-7825(82)90128-1

23. G. G. Chew, I. C. Howard, E. A. Patterson, Simulation of damage in a porcine prosthetic heart valve, *J. Med. Eng. Technol.*, **23** (1999), 178–189. https://doi.org/10.1080/030919099294131

24. J. De Hart, G. W. M. Peters, P. J. G. Schreurs, F. P. T. Baaijens, A three-dimensional computational analysis of fluid–structure interaction in the aortic valve, *J. Biomech.*, **36** (2003), 103–112. https://doi.org/10.1016/S0021-9290(02)00244-0

25. C. S. Peskin, The immersed boundary method, *Acta Numer.*, **11** (2002), 479–517. https://doi.org/10.1017/S0962492902000077

26. B. E. Griffith, Immersed boundary model of aortic heart valve dynamics with physiological driving and loading conditions, *Int. J. Numer. Methods Biomed. Eng.*, **28** (2012), 317–345. https://doi.org/10.1002/cnm.1445

27. X. Ma, H. Gao, B. E. Griffith, C. Berry, X. Luo, Image-based fluid–structure interaction model of the human mitral valve, *Comput. Fluids*, **71** (2013), 417–425. https://doi.org/10.1016/j.compfluid.2012.10.025

28. H. Gao, X. Ma, N. Qi, C. Berry, B. E. Griffith, X. Luo, A finite strain nonlinear human mitral valve model with fluid-structure interaction, *Int. J. Numer. Methods Biomed. Eng.*, **30** (2014), 1597–1613. https://doi.org/10.1002/cnm.2691

29. H. Gao, N. Qi, L. Feng, X. Ma, M. Danton, C. Berry, et al., Modelling mitral valvular dynamics–current trend and future directions, *Int. J. Numer. Methods Biomed. Eng.*, **33** (2017), e2858. https://doi.org/10.1002/cnm.2858

30. B. E. Griffith, X. Luo, Hybrid finite difference/finite element immersed boundary method, *Int. J. Numer. Methods Biomed. Eng.*, **33** (2017), e2888. https://doi.org/10.1002/cnm.2888

31. H. Gao, L. Feng, N. Qi, C. Berry, B. E. Griffith, X. Luo, A coupled mitral valve—left ventricle model with fluid–structure interaction, *Med. Eng. Phys.*, **47** (2017), 128–136. https://doi.org/10.1016/j.medengphy.2017.06.042

32. A. Hasan, E. M. Kolahdouz, A. Enquobahrie, T. G. Caranasos, J. P. Vavalle, B. E. Griffith, Image-based immersed boundary model of the aortic root, *Med. Eng. Phys.*, **47** (2017), 72–84. https://doi.org/10.1016/j.medengphy.2017.05.007

33. L. Cai, Y. Wang, H. Gao, X. Ma, G. Zhu, R. Zhang, et al., Some effects of different constitutive laws on fsi simulation for the mitral valve, *Sci. Rep.*, **9** (2019), 12753. https://doi.org/10.1038/s41598-019-49161-6

34. L. Cai, R. Zhang, Y. Li, G. Zhu, X. Ma, Y. Wang, et al., The comparison of different constitutive laws and fiber architectures for the aortic valve on fluid–structure interaction simulation, *Front. Physiol.*, **12** (2021), 725. https://doi.org/10.3389/fphys.2021.682893

35. L. Feng, H. Gao, B. Griffith, S. Niederer, X. Luo, Analysis of a coupled fluid-structure interaction model of the left atrium and mitral valve, *Int. J. Numer. Methods Biomed. Eng.*, **35** (2019), e3254. https://doi.org/10.1002/cnm.3254

36. L. Feng, H. Gao, N. Qi, M. Danton, N. A. Hill, X. Luo, Fluid–structure interaction in a fully coupled three-dimensional mitral–atrium–pulmonary model, *Biomech. Model. Mechanobiol.*, **20** (2021), 1267–1295. https://doi.org/10.1007/s10237-021-01444-6

37. J. H. Lee, L. N. Scotten, R. Hunt, T. G. Caranasos, J. P. Vavalle, B. E. Griffith, Bioprosthetic aortic valve diameter and thickness are directly related to leaflet fluttering: results from a combined experimental and computational modeling study, *JTCVS Open*, **6** (2021), 60–81. https://doi.org/10.1016/j.xjon.2020.09.002

38. M. J. Thubrikar, J. Aouad, S. P. Nolan, Patterns of calcific deposits in operatively excised stenotic or purely regurgitant aortic valves and their relation to mechanical stress, *Am. J. Cardiol.*, **58** (1986), 304–308. https://doi.org/10.1016/0002-9149(86)90067-6

39. G. Zhu, M. Nakao, Q. Yuan, J. H. Yeo, In-vitro assessment of expanded-polytetrafluoroethylene stentless tri-leaflet valve prosthesis for aortic valve replacement, in *Biodevices*, (2017), 186–189.

40. C. M. Otto, Calcific aortic stenosis—time to look more closely at the valve, *N. Engl. J. Med.*, **359** (2008), 1395–1398. https://doi.org/10.1056/NEJMe0807001

41. C. Russ, R. Hopf, S. Hirsch, S. Sündermann, V. Falk, G. Székely, et al., Simulation of transcatheter aortic valve implantation under consideration of leaflet calcification, in *2013 35th Annual International Conference of the IEEE Engineering in Medicine and Biology Society (EMBC)*, (2013), 711–714. https://doi.org/10.1109/EMBC.2013.6609599

42. Q. Wang, S. Kodali, C. Primiano, W. Sun, Simulations of transcatheter aortic valve implantation: implications for aortic root rupture, *Biomech. Model. Mechanobiol.*, **14** (2015), 29–38. https://doi.org/10.1007/s10237-014-0583-7

43. E. P. Van Der Poel, R. Ostilla-Mónico, J. Donners, R. Verzicco, A pencil distributed finite difference code for strongly turbulent wall-bounded flows, *Comput. Fluids*, **116** (2015), 10–16. https://doi.org/10.1016/j.compfluid.2015.04.007

44. A. Farina, L. Fusi, A. Mikeli, G. Saccomandi, E. F. Toro, *Non-Newtonian Fluid Mechanics and Complex Flows*, 2018.

45. P. D. Morris, A. Narracott, H. von Tengg-Kobligk, D. A. S. Soto, S. Hsiao, A. Lungu, et al., Computational fluid dynamics modelling in cardiovascular medicine, *Heart*, **102** (2016), 18–28. http://dx.doi.org/10.1136/heartjnl-2015-308044

46. H. Gao, D. Carrick, C. Berry, B. E. Griffith, X. Luo, Dynamic finite-strain modelling of the human left ventricle in health and disease using an immersed boundary-finite element method, *IMA J. Appl. Math.*, **79** (2014), 978–1010. https://doi.org/10.1093/imamat/hxu029

47. S. Land, V. Gurev, S. Arens, C. M. Augustin, L. Baron, R. Blake, et al., Verification of cardiac mechanics software: benchmark problems and solutions for testing active and passive material behaviour, *Proc. R. Soc. A*, **471** (2015), 20150641. https://doi.org/10.1098/rspa.2015.0641

48. S. Katayama, N. Umetani, T. Hisada, S. Sugiura, Bicuspid aortic valves undergo excessive strain during opening: a simulation study, *J. Thorac. Cardiovasc. Surg.*, **145** (2013), 1570–1576. https://doi.org/10.1016/j.jtcvs.2012.05.032

49. N. Stergiopulos, B. E. Westerhof, N. Westerhof, Total arterial inertance as the fourth element of the windkessel model, *Am. J. Physiol.-Heart Circ. Physiol.*, **276** (1999), H81–H88. https://doi.org/10.1152/ajpheart.1999.276.1.H81

50. G. Zhu, M. B. Ismail, M. Nakao, Q. Yuan, J. H. Yeo, Numerical and in-vitro experimental assessment of the performance of a novel designed expanded-polytetrafluoroethylene stentless bi-leaflet valve for aortic valve replacement, *PLoS One*, **14** (2019), e0210780. https://doi.org/10.1371/journal.pone.0210780

51. A. P. Yoganathan, Z. He, S. C. Jones, Fluid mechanics of heart valves, *Annu. Rev. Biomed. Eng.*, **6** (2004), 331–362. https://doi.org/10.1146/annurev.bioeng.6.040803.140111

52. P. N. Jermihov, L. Jia, M. S. Sacks, R. C. Gorman, J. H. Gorman, K. B. Chandran, Effect of geometry on the leaflet stresses in simulated models of congenital bicuspid aortic valves, *Cardiovasc. Eng. Technol.*, **2** (2011), 48–56. https://doi.org/10.1007/s13239-011-0035-9

53. A. M. Mohammed, M. Ariane, A. Alexiadis, Using discrete multiphysics modelling to assess the effect of calcification on hemodynamic and mechanical deformation of aortic valve, *ChemEngineering*, **4** (2020), 48. https://doi.org/10.3390/chemengineering4030048

54. M. J. Thubrikar, *The Aortic Valve*, 1990.

55. R. O. Bonow, B. A. Carabello, K. Chatterjee, A. C. De Leon, D. P. Faxon, M. D. Freed, et al., ACC/AHA 2006 guidelines for the management of patients with valvular heart disease: a report of the american college of cardiology/american heart association task force on practice guidelines (writing committee to revise the 1998 guidelines for the management of patients with valvular heart disease): developed in collaboration with the society of cardiovascular anesthesiologists endorsed by the society for cardiovascular angiography and interventions and the society of thoracic surgeons, *Circulation*, **114** (2006), e84–e231. https://doi.org/10.1161/CIRCULATIONAHA.106.176857

56. R. A. Nishimura, C. M. Otto, R. O. Bonow, B. A. Carabello, J. P. Erwin, R. A. Guyton, et al., 2014 AHA/ACC guideline for the management of patients with valvular heart disease: executive summary, a report of the american college of cardiology/american heart association task force on practice guidelines, *Circulation*, **129** (2014), 2440–2492. https://doi.org/10.1161/CIR.0000000000000029

57. R. A Nishimura, C. M. Otto, R. O. Bonow, B. A. Carabello, J. P. Erwin, L. A. Fleisher, et al., 2017 AHA/ACC focused update of the 2014 aha/acc guideline for the management of patients with valvular heart disease: a report of the american college of cardiology/american heart association task force on clinical practice guidelines, *J. Am. Coll. Cardiol.*, **70** (2017), 252–289. https://doi.org/10.1016/j.jacc.2017.03.011

58. H. Baumgartner, J. Hung, J. Bermejo, J. B. Chambers, A. Evangelista, B. P. Griffin, et al., Echocardiographic assessment of valve stenosis: Eae/ase recommendations for clinical practice, *Eur. J. Echocardiography*, **10** (2009), 1–25. https://doi.org/10.1093/ejechocard/jen303

59. W. W. Chen, H. Gao, X. Y. Luo, N. A. Hill, Study of cardiovascular function using a coupled left ventricle and systemic circulation model, *J. Biomech.*, **49** (2016), 2445–2454. https://doi.org/10.1016/j.jbiomech.2016.03.009

60. D. Garcia, P. Pibarot, L. Kadem, L. G. Durand, Respective impacts of aortic stenosis and systemic hypertension on left ventricular hypertrophy, *J. Biomech.*, **40** (2007), 972–980. https://doi.org/10.1016/j.jbiomech.2006.03.020

61. E. J. Weinberg, F. J. Schoen, M. R. K. Mofrad, A computational model of aging and calcification in the aortic heart valve, *PLoS One*, **4** (2009), e5960. https://doi.org/10.1371/journal.pone.0005960

62. Y. Geng, H. Liu, X. Wang, J. Zhang, Y. Gong, D. Zheng, et al., Effect of microcirculatory dysfunction on coronary hemodynamics: a pilot study based on computational fluid dynamics simulation, *Comput. Biol. Med.*, **146** (2022), 105583. https://doi.org/10.1016/j.compbiomed.2022.105583

63. H. Liu, L. Lan, J. Abrigo, H. L. Ip, Y. Soo, D. Zheng, et al., Comparison of newtonian and non-newtonian fluid models in blood flow simulation in patients with intracranial arterial stenosis, *Front. Physiol.*, **12** (2021), 718540. https://doi.org/10.3389/fphys.2021.718540

64. F. De Vita, M. D. De Tullio, R. Verzicco, Numerical simulation of the non-newtonian blood flow through a mechanical aortic valve, *Theor. Comput. Fluid Dyn.*, **30** (2016), 129–138. https://doi.org/10.1007/s00162-015-0369-2

65. I. Pericevic, C. Lally, D. Toner, D. J. Kelly, The influence of plaque composition on underlying arterial wall stress during stent expansion: the case for lesion-specific stents, *Med. Eng. Phys.*, **31** (2009), 428–433. https://doi.org/10.1016/j.medengphy.2008.11.005